

Bosonic Confinement and Coherence in Disordered Nanodiamond Arrays

Gufei Zhang,^{*,§,||} Tomas Samuely,^{#,||} Hongchu Du,^{†,‡,||} Zheng Xu,[⊥] Liwang Liu,[∇] Oleksandr Onufriienko,[#] Paul W. May,[○] Johan Vanacken,[§] Pavol Szabó,[#] Jozef Kačmarčík,[#] Haifeng Yuan,^{||} Peter Samuely,[#] Rafal E. Dunin-Borkowski,^{†,+} Johan Hofkens,^{||,ⓑ} and Victor V. Moshchalkov^{*,§}

[§]INPAC-Institute for Nanoscale Physics and Chemistry, KU Leuven, Celestijnenlaan 200D, B-3001 Heverlee, Belgium

[#]Centre of Low Temperature Physics, Institute of Experimental Physics, Slovak Academy of Sciences, and Faculty of Science, P. J. Safarik University, 04001 Kosice, Slovakia

[†]Ernst Ruska Centre for Microscopy and Spectroscopy with Electrons, Forschungszentrum Jülich GmbH, Jülich 52425, Germany

[‡]Central Facility for Electron Microscopy, RWTH Aachen University, Aachen 52074, Germany

[⊥]School of Electrical and Computer Engineering, University of California, Davis, California 95616, United States

[∇]University of Bordeaux, CNRS, UMR 5295, I2M, F-33400 Talence, France

[○]School of Chemistry, University of Bristol, Bristol BS8 1TS, United Kingdom

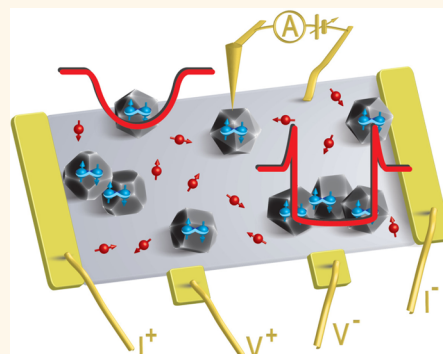
^{||}Department of Chemistry, KU Leuven, Celestijnenlaan 200F, B-3001 Heverlee, Belgium

⁺Peter Grünberg Institute, Forschungszentrum Jülich GmbH, 52425 Jülich, Germany

Supporting Information

ABSTRACT: In the presence of disorder, superconductivity exhibits short-range characteristics linked to localized Cooper pairs which are responsible for anomalous phase transitions and the emergence of quantum states such as the bosonic insulating state. Complementary to well-studied homogeneously disordered superconductors, superconductor-normal hybrid arrays provide tunable realizations of the degree of granular disorder for studying anomalous quantum phase transitions. Here, we investigate the superconductor–bosonic dirty metal transition in disordered nanodiamond arrays as a function of the dispersion of intergrain spacing, which ranges from angstroms to micrometers. By monitoring the evolved superconducting gaps and diminished coherence peaks in the single-quasiparticle density of states, we link the destruction of the superconducting state and the emergence of bosonic dirty metallic state to breaking of the global phase coherence and persistence of the localized Cooper pairs. The observed resistive bosonic phase transitions are well modeled using a series–parallel circuit in the framework of bosonic confinement and coherence.

KEYWORDS: nanodiamond, amorphous carbon, disordered hybrid arrays, confinement and coherence, superconducting order parameter



Diamond grown by chemical vapor deposition (CVD) has recently drawn considerable attention due to its properties such as the extraordinarily high thermal conductivity, breakdown voltage, and stiffness, which open perspectives for the applications of this material in the next-generation electronics.¹ Diamond field-effect transistors and microelectro-mechanical radio frequency switches have been demonstrated to be superior candidates for high-power high-speed devices,^{2,3} while diamond-GaN composite devices offer significant performance-enhancing potential for active and passive future high-power radio frequency and microwave communications devices.⁴

Apart from its perspectives for electrical and electronic engineering, CVD diamond with wide ranging electronic properties provides a powerful platform for fundamental research.⁵ The electrical conductivity of CVD diamond can be tuned using boron as a *p*-type dopant which can be added to the gas mixture during the CVD process. As the boron concentration increases, the diamond changes from highly insulating when undoped, through semiconducting when lightly

Received: October 9, 2017

Accepted: November 10, 2017

Published: November 10, 2017

doped, to metallic when heavily doped. With even further increase of the boron concentration, the diamond appears black and exhibits superconductivity.^{6,7} This discovery has not only resulted in the realization of diamond-based superconducting quantum interference device (SQUID)⁸ but also revived the interest in the counterintuitive correlation between the *good* superconductivity and *bad* conductor nature of doped insulators.^{5,9,10}

Another contribution of superconducting diamond to physics research is based on its granular disorder.^{5,11} Since the discovery of superconductivity, the influence of disorder on the quantum condensate of charged bosons has remained a subject of interest, for which homogeneously disordered superconductors have been extensively studied,^{12–16} and theoretically modeled by Josephson junction arrays.¹⁵ Research on such systems has boosted our understanding of the formation and behaviors of Cooper pairs by demonstrating anomalous phase transitions and quantum states such as the bosonic insulating state.¹⁵ In contrast to the achievements in homogeneously disordered superconductors, research carried out on granular disordered systems is still rather limited.^{17,18} Meanwhile, studies of the Josephson coupling in nanostructured systems have also drawn considerable attention. For instance, two-dimensional Josephson junction arrays have been nanofabricated to study the dissipation-driven superconductor–insulator transition, charge solitons, and quantum fluctuations.^{19,20} Positional disorder has been introduced into superconducting wire networks and Josephson junction arrays to theoretically modulate the magnetic-field-dependent oscillations of the superconducting transition temperature.²¹ Amorphous Bi has been grown on nanohoneycomb-structured aluminum oxide to study the bosonic insulating state as a function of the film thickness.²² Recently, Nb–Au–Nb and Sn–graphene–Sn hybrid arrays have been independently used to study the zero-temperature metallic states in two dimensions.^{23,24} Despite the flexibility of the top-down approach for the nanofabrication of the superconducting dot arrays, an important factor, that is, dot site disorder, cannot be properly introduced into the structures due to the incompatibility between the periodic design for lithography and the random nature of disorder. In contrast to lithography, the preliminary seeding procedure, used for the chemical vapor deposition of diamond, makes the sample preparation a bottom-up process (see [Experimental Section](#)),¹ in which the randomly distributed nanodiamond seeds (nucleation sites for the diamond growth) naturally serve as disorder centers.

Here, we report on our investigations of bosonic confinement and coherence in a set of disordered nanodiamond arrays situated in the three-dimensional (3D) regime. The dispersed intergrain spacing results in the isolation and Josephson coupling of nanodiamonds at different locations and thus gives rise to anomalous resistive superconducting transitions and bosonic dirty metallic states at low temperatures. Our direct local measurements of the density of states (DOS) reveal a broad distribution of the local critical temperature of different nanodiamonds and provide direct evidence for the formation of precursor Cooper pairs well above the superconducting transition temperature. The superconducting gaps, observed in isolated nanodiamonds, demonstrate no coherence peaks in the DOS, suggesting the absence of a long-range superconducting state and thus localization of the preformed Cooper pairs in these grains. The anomalous resistive superconducting transitions are interpreted in the framework of a semiempirical

model taking into account the disorder-induced bosonic confinement and coherence.

RESULTS AND DISCUSSION

Our samples include two disordered arrays of nanodiamond particles and a continuous diamond film made up of connected nanodiamond crystallites grown on Si/SiO₂ substrates, which are labeled as NDA1, NDA2, and CDF, respectively (see [Figure 1](#)). NDA1 and NDA2 consist of sparse nanodiamonds of mean

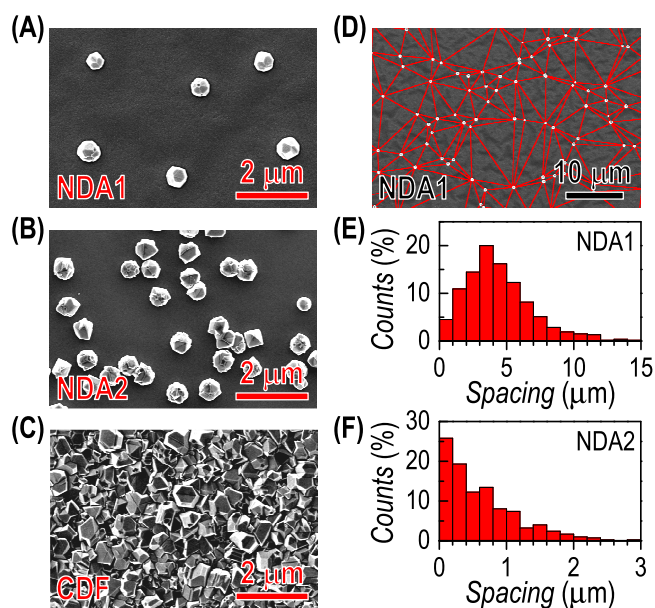


Figure 1. SEM images of disordered nanodiamond–DLC hybrid arrays and statistics of intergrain spacing. (A–C) SEM images of NDA1 (A), NDA2 (B), and CDF (C). (D) Triangular tessellation (red lines) of SEM image for statistical analysis of the spacings between the nanodiamonds (white dots). The DLC underneath the nanodiamonds show wrinkled features. (E and F) Statistics of the intergrain spacings of NDA1 (E) and NDA2 (F).

size ~ 500 – 600 nm, sitting on and partially embedded in a layer of 180 nm-thick amorphous carbon/diamond-like carbon (DLC), which acts as the electrical connection between the boron-doped grains. The mean intergrain spacings S of NDA1 and NDA2 are estimated to be $4.4 \mu\text{m}$ and 620 nm, respectively (see [Figure 1D–F](#)). In contrast, CDF is composed of a dense polycrystalline film containing many diamond crystallites which have fused together to form a continuous layer following growth on initial seed crystals during the CVD process. In this sample, electrical connection between the boron-doped grains is *via* the interface where crystallites meet at grain boundaries. These thin (~ 2 Å) columnar grain boundaries contain a mixture of sp^2 and sp^3 carbon-bonding types as well as impurity atoms of boron. Taking into account the 3D nature of all samples and the similar composition of the grain boundaries in CDF and the DLC layer in NDA, CDF can be viewed as a third nanodiamond array with $S \sim 2$ Å and serves as a reference sample with which to compare the two NDA films. The same fabrication parameters were used for the preparation of all three samples to ensure that the mean grain size (~ 500 – 600 nm) (see [Supporting Information Figure S1](#)) and boron doping level ($\sim 2 \times 10^{21} \text{ cm}^{-3}$) of the arrays do not differ significantly in all samples, leaving the dispersion of the intergrain spacing the

only key variable (see [Experimental Section](#) for fabrication details).

Structural analysis of the disordered nanodiamond arrays was carried out using annular dark-field scanning transmission electron microscopy (ADF-STEM) and spatially resolved electron energy-loss spectroscopy (STEM-EELS).⁵ [Figure 2](#)

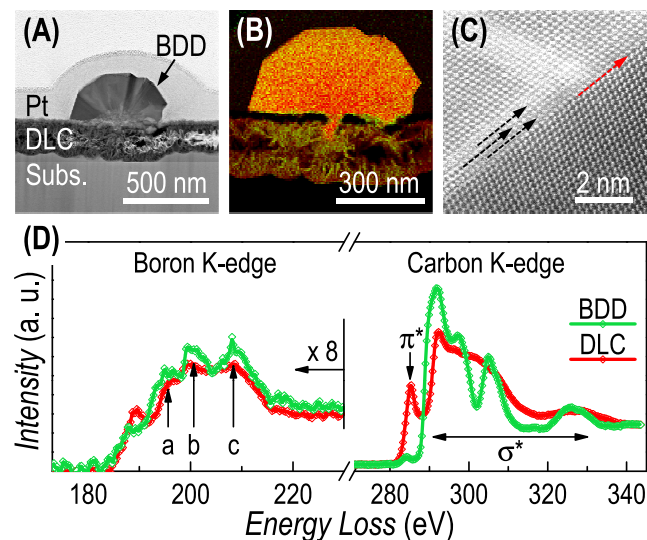


Figure 2. STEM-EELS measurements and ADF-STEM imaging of nanodiamonds. (A) ADF-STEM image of the cross-section of NDA. (B) STEM-EELS spectrum imaging of boron (in green) and carbon (in red) distributions in NDA, displayed from the threshold minima at the Pt-layer to their respective maxima. The superposition of green and red pixels results in the yellow/orange color of the BDD and DLC. (C) High-resolution ADF-STEM image showing the lattice fringes, stacking faults (black arrows), and one of the twin boundaries (red arrow) in the polycrystalline nanodiamond. (D) Characteristic EELS spectra recorded from BDD and DLC. In nanodiamonds, the subpeaks (a–c) of the boron K-edge, corresponding to the fine structure of the carbon K-edge, indicate the tetrahedral coordination (substitutional doping) of boron in diamond. In DLC, the mismatch between the fine structures of the boron K-edge and carbon K-edge is indicative of boron-enriched amorphous carbon.

shows the structural analysis data obtained from the characteristic cross-section of NDA. The DLC layer is about 180 nm thick and decorated with boron-doped nanodiamonds (BDD) (see [Figure 2A](#)). Spatially resolved STEM-EELS measurements indicate a rather homogeneous boron concentration of $\sim 2 \times 10^{21} \text{ cm}^{-3}$ for the tetrahedrally coordinated boron atoms in BDD, which is one order of magnitude higher than the critical doping level for the insulator–metal transition in diamond.²⁵ Due to superposition of carbon (red pixels) and boron (green pixels) signals in elemental mapping, the BDD appears yellow/orange in [Figure 2B](#). As revealed by high-resolution TEM, the black nanodiamonds are polycrystalline and rich in crystallographic defects such as twin boundaries (see [Figure 2C](#)). Although boron atoms are also incorporated in the DLC with a concentration of $\sim 1 \times 10^{21} \text{ cm}^{-3}$, the fine structures of the boron K-edge and carbon K-edge in the characteristic EELS spectra show that the boron atoms are mainly coordinated in an amorphous form, together with the sp^2 and sp^3 mixtures of carbon (see [Figure 2D](#)).⁵

[Figure 3](#) shows the thermoresistivity $\rho(T)$ of the disordered nanodiamond arrays. In contrast to the rather common

superconducting transition observed around $T_c \sim 3 \text{ K}$ in CDF, NDA1 and NDA2 demonstrate anomalous phase transitions at low temperatures. In addition to the monotonic increase of resistivity, when decreasing the temperature, a kink is found in the $\rho(T)$ curve of NDA1 around the T_c observed for CDF. At about the same temperature, a more pronounced phase transition with a positive temperature coefficient of resistivity is observed in NDA2. When decreasing the temperature further, the negative temperature coefficient of resistivity is resumed, giving rise to a $\rho(T)$ dip at 2 K.

To confirm the bosonic nature of the resistivity kink and dip observed in NDA1 and NDA2, respectively, we measured the thermoresistivity in different applied magnetic fields. As shown in [Figure 3B](#), the resistivity anomalies of these two nanodiamond arrays are both suppressed in higher magnetic fields. A deeper comprehension of these bosonic resistive phase transitions requires analysis of the intergrain coupling in the arrays. It is well-known that in superconductor-normal metal-superconductor arrays, the superconducting order parameter extends into the normal conductor by a distance of b , which is a rather complex parameter dependent on many factors such as the structure of the array, the temperature, and the DOS in the superconductors and the normal conductor.²⁶ In practice, the coherence length ξ_N of the normal conductor is generally taken as an approximation of b and for comparison with the separation of the superconductors.^{23,27} Using the Einstein relation, the diffusion coefficient D of our DLC is estimated to be $37.3 \text{ cm}^2 \text{ s}^{-1}$ at 3 K (see [Experimental Section](#)), which in the dirty limit yields a ξ_N of 97 nm following:²⁸

$$\xi_N = \sqrt{\frac{\hbar D}{2\pi k_B T}} \quad (1)$$

The resulting ξ_N/S ratios are, therefore, 0.02 for NDA1, 0.2 for NDA2, and 485 for CDF.

In NDA1, the nanodiamonds are mostly well separated from each other. At low temperatures, intragrain Cooper pairing sets in, giving rise to the formation of localized bosonic islands at the nanodiamond scale. The localized bosonic islands contribute to the electrical transport by acting as local current sinks in the framework of the Andreev reflection. In the absence of phase coherence between the localized bosonic islands, NDA1 demonstrates a dirty metallic state rather than a superconducting state ($\rho = 0$) at low temperatures, which mainly results from the disordered DLC. Despite the rather small ξ_N/S ratio of NDA2, locally dense nanodiamond aggregations are found in this array (see [Figure 1B,F](#)). Due to the formation of nanodiamond-DLC-nanodiamond Josephson junctions, local phase coherence is established between the aggregated nanodiamonds, resulting in the resistivity drop around 3 K (see [Figure 3B](#)). The $\rho(T)$ dip evolves into a kink and smears out in applied magnetic fields. The remarkably large ξ_N/S ratio of CDF indicates that proximity coupling between the nanodiamonds leads to global phase coherence and thus the presence of the superconducting state $\rho = 0$ in the system (see [Figure 3B](#)). Based on the magnetic-field dependence of $\rho(T)$, we construct the $\mu_0 H_{c2} - T$ phase diagram for CDF, from which the zero-temperature upper critical field $\mu_0 H_{c2}(0 \text{ K}) = 4.15 \text{ T}$ and the Ginzburg–Landau coherence length $\xi_{GL} = 8.9 \text{ nm}$ are deduced (see [Supporting Information Figure S2](#)).

By applying a relatively high magnetic field of 5 T, the phase coherence between the nanodiamonds is destroyed, and the majority of the Cooper pairs are broken, bringing out the

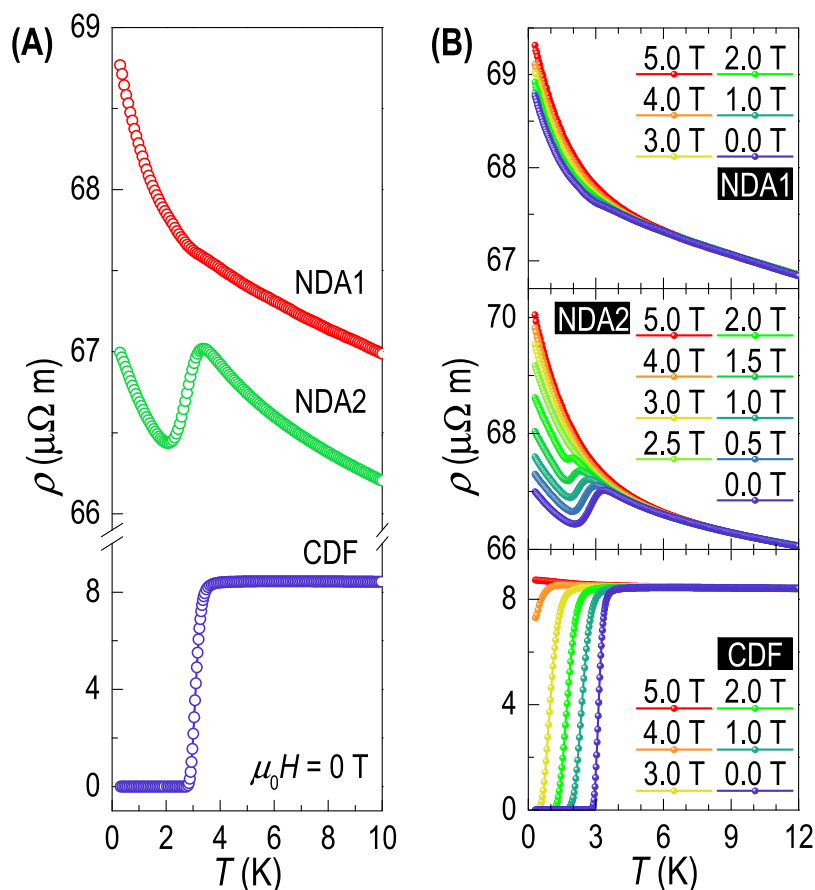


Figure 3. Bosonic resistive phase transitions in disordered nanodiamond arrays. (A) CDF shows a typical superconducting transition around 3 K, while NDA1 and NDA2 demonstrate bosonic resistive phase transitions with a kink and a resistivity drop, respectively, at about the same temperature. (B) Similar to CDF, the resistive phase transitions in NDA1 and NDA2 are suppressed in applied magnetic fields as well, indicating the bosonic nature of the transitions.

influence of the DLC on the electrical transport in the arrays.

As shown in Figure 4, at high temperatures, the $\rho(T)|_{5\text{ T}}$ curves

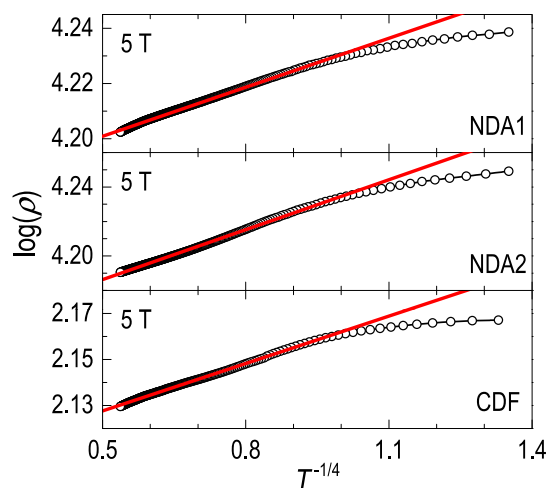


Figure 4. Analysis of the fermion hopping mechanism in disordered nanodiamond arrays. The influence of the DLC on the electrical transport is brought out by suppressing the contribution from the superconducting nanodiamonds with an applied magnetic field of 5 T. Above 1 K, the experimental data (black circles) are in good agreement with Mott's law in 3D (red lines).

are found to be in a good agreement with 3D Mott's law (variable range hopping):²⁹

$$\rho = \rho_0 \exp\left\{\left(\frac{T_0}{T}\right)^{1/4}\right\} \quad (2)$$

where T_0 characterizes the strength of single quasiparticle correlation. Below 1 K, the increase in $\rho(T)|_{5\text{ T}}$ slows down, and the curves deviate from the theory, suggesting the presence of remnant superconductivity in the arrays.

Above we interpreted the anomalous bosonic phase transitions in NDA1 and NDA2 in terms of confinement and coherence of the superconducting order parameter based on electrical transport measurements, which characterize the macroscopic properties of the nanodiamond arrays. To complete our physics picture, scanning tunneling microscopy/spectroscopy (STM/S) was employed to measure the local modulations of the superconducting order parameter. Meanwhile, taking advantage of the NDA, in which black nanodiamonds and boron-enriched DLC are separated, the STM/S measurements should close the debate on the origin of superconductivity in polycrystalline diamond,³⁰ that is, it is the substitutional boron doping of diamond rather than the boron enrichment of amorphous carbon originating the superconductivity.

Figure 5 presents the characteristic normalized differential conductance spectra $G_{\text{norm}}(V_b)$ recorded from the nano-

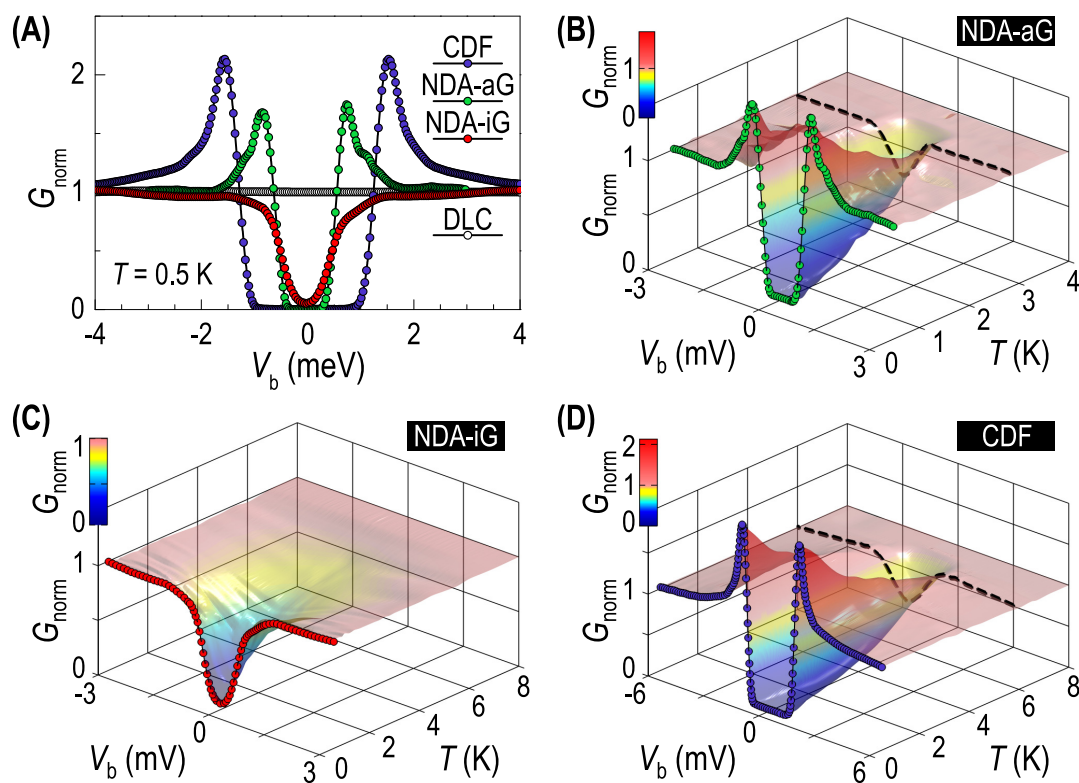


Figure 5. Characteristic differential conductance spectra demonstrating the long- and short-range superconductivity in CDF and NDA, respectively. (A) Normalized tunneling conductance G_{norm} as a function of bias voltage V_b shows the absence of superconductivity in the DLC away from the nanodiamonds. In CDF, only U-shaped $G_{\text{norm}}(V_b)$ gaps with giant coherence peaks are observed, while in NDA, two sorts of gaps are found, that is, U-shaped NDA-aG with diminished coherence peaks in aggregated nanodiamonds and NDA-iG with a shape in between U and V and without coherence peaks at all in isolated nanodiamonds. At 0.5 K, the half width of the superconducting gaps of NDA-aG, NDA-iG, and CDF is 0.75, 0.87, and 1.45 meV, respectively. (B–D) Temperature-induced evolution of the characteristic differential conductance spectra. The reduced coherence peak height and the U-to-V shape transformation of the superconducting gap indicate that the long-range superconductivity evolves into a short-range ordering, due to breaking of global phase coherence.

diamond arrays. Our data clearly show the absence of superconductivity in the boron-enriched DLC (see Figure 5A). When measuring the black nanodiamonds in NDA1 and NDA2, two types of $G_{\text{norm}}(V_b)$ spectra are observed: the aggregated nanodiamonds demonstrate U-shaped superconducting gaps with relatively large coherence peaks (see NDA-aG in Figure 5A,B), while the isolated nanodiamonds show superconducting gaps with a shape in between U and V and without coherence peaks (see NDA-iG in Figure 5A,C). In contrast to the sparse nanodiamonds, CDF demonstrates only one type of superconducting gap, that is, U-shaped gaps with giant coherence peaks (see Figure 5A,D). Note that the coherence peak height (CPH), directly linked to the local phase coherence, can be taken as a measure of the disorder degree of a superconductor.^{16,31}

In the case of strong bosonic confinement, the lost spectral weight due to the opening of the superconducting gap will not be added to the edges of the gap, leaving behind a gapped $G_{\text{norm}}(V_b)$ spectrum without coherence peaks.^{16,31} Hence, the superconducting gaps free of coherence peaks (see NDA-iG in Figure 5A,C), observed in the isolated nanodiamonds of NDA1 and NDA2, could be due to strong intragrain confinement of Cooper pairs, which becomes feasible when the grain size is effectively reduced by the intragrain crystallographic defects such as twin boundaries. The confinement of Cooper pairs in the isolated nanodiamonds is further evidenced by their much

higher upper critical field than the bulk value (see Supporting Information Figure S3).

Furthermore, although V- and U-shaped superconducting gaps have been previously reported for diamonds with different crystalline orientations, that is, V-shaped gaps for (111)-oriented crystals and U-shaped for (100)-oriented crystals,³² this correlation is not found by our STM/S data. Note that our CDF is polycrystalline and has a preferential crystalline orientation in the (111) direction (see the triangular facets in Figure 1C), while no V-shaped gap is observed in our thorough search of different areas of the CDF. Taking into account the exclusive emergence of U-shaped gaps in the CDF (see Figure 5A,D), we consider global phase coherence and local phase decoherence as the cause of the U- and V-shaped superconducting gaps, respectively.

In the framework of our physics picture, U-shaped gaps should gradually evolve into V-shaped ones with diminished coherence peaks, when increasing the degree of disorder and/or the temperature of a system. Similar to disorder, the increase of temperature breaks the global phase coherence as well. The temperature-induced evolution of the $G_{\text{norm}}(V_b)$ spectra shows exactly such U–V transformations of the superconducting gap in our disordered nanodiamond arrays (see dashed curves in Figure 5B,D). Note that research on InO films has shown the change of the superconducting gap from U to a shape in between U and V, due to the increased degree of disorder.¹⁶ In

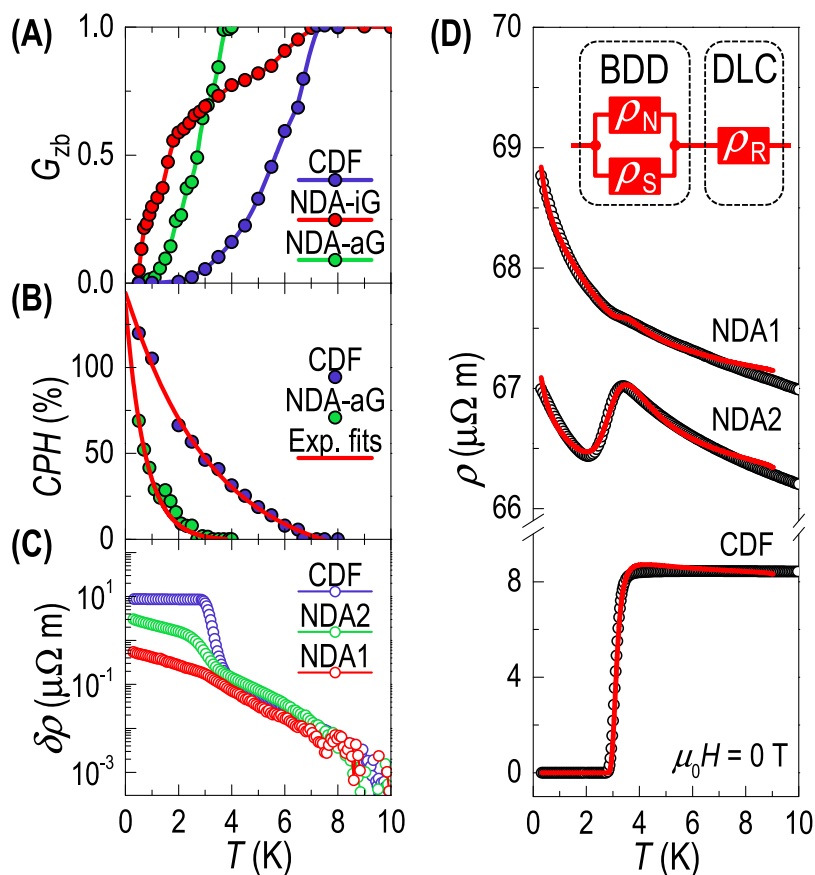


Figure 6. Formation of localized precursor Cooper pairs and modeling of the bosonic resistive phase transitions. (A–C) Temperature dependences of the zero-bias tunneling conductance G_{zb} (A), the coherence peak height CPH (B), and the resistivity difference $\delta\rho = \rho|_{5\text{ T}} - \rho|_{0\text{ T}}$ (C). The $G_{zb}(T)$ plots demonstrate a broad distribution of the local critical temperature, and the temperature dependence of CPH indicates that the phase coherence exponentially decays when increasing temperature. Above 9 K, the $\delta\rho(T)$ plots become discontinuous on the semilogarithmic scale due to the emergence of negative values caused by experimental noise. Accordingly, $T = 9$ K is taken as the onset critical temperature of the bosonic resistive phase transitions. The $G_{zb}(T) < 1$ and $CPH = 0$, observed in isolated nanodiamonds such as NDA-iG well above 3 K, reveal the formation of localized precursor Cooper pairs. (D) Theoretical modeling (red curves) of the bosonic resistive phase transitions (black circles) by a series–parallel combination circuit, in which a single quasiparticle resistor ρ_N and a “superconducting” resistor ρ_S are connected in parallel to mimic the BDD, and the third resistor ρ_R represents the DLC.

the same research, U-shaped gaps also evolved into V-shaped ones when increasing the temperature.¹⁶

When plotting the local measurement results and the global electrical transport properties together, further insight can be gained into the localization of the preformed Cooper pairs and the onset of the resistive superconducting transitions. The zero-bias conductance G_{zb} and CPH , extracted from the temperature-induced evolution of the $G_{\text{norm}}(V_b)$ spectra, are plotted as a function of temperature in Figure 6A,B, respectively. From the $G_{zb}(T)$ plots, the local critical temperature of NDA-iG, NDA-aG, and CDF is determined. With the zero-temperature superconducting gap $2\Delta_0$ estimated from Figure 5, the $2\Delta_0/k_B T_c$ ratio is deduced to be 2.88, 4.46, and 4.67 for NDA-iG, NDA-aG, and CDF, respectively. To determine the onset critical temperature T_c^{onset} of the bosonic phase transitions, $\delta\rho(T) = \rho(T)|_{5\text{ T}} - \rho(T)|_{0\text{ T}}$ is plotted on a semilogarithmic scale in Figure 6C, and $\delta\rho(T) = 0$ is set as the criterion for the determination of T_c^{onset} . This criterion setting provides the closest estimate of T_c^{onset} by taking into account the superconducting fluctuation regime prior to the resistive superconducting transition.³³ Accordingly, T_c^{onset} is found to be 8.8, 9.0, and 9.1 K for NDA1, NDA2, and CDF, respectively. The T_c^{onset} values with a negligible deviation within the limits of

experimental error are indicative of similar boron concentration in the samples. The distinct difference between T_c^{onset} and the offset critical temperature $T_c^{\text{offset}} = 2.8$ K of CDF indicates the formation of precursor Cooper pairs and suggests a broad distribution of the local critical temperature, which are both confirmed by the temperature dependence of G_{zb} and CPH .

Based on Figure 6A–C, we interpret the bosonic phase transitions as follows: Cooper pairing sets in at T_c^{onset} , while, in the presence of disorder, the precursor Cooper pairs are localized and isolated. With decreasing temperatures, localized bosonic islands are formed, which separately contribute to the electrical transport, and demonstrate fairly weak influence on the resistivity. Further decrease in temperature brings about the growth of the bosonic islands, the formation of more bosonic islands, and the intervention of local phase coherence, giving rise to the kink in NDA1 and the resistivity drop in NDA2 and CDF. In the case of the establishment of global phase coherence at even lower temperatures, a global superconducting state ($\rho = 0$) will be developed such as in CDF. Otherwise, the localized bosonic islands will continue to grow but still remain in isolation, thus turning the system into a bosonic dirty metal such as NDA1 and NDA2.

Table 1. Variables Used for Modeling the Disordered Nanodiamond Arrays with the Series–Parallel Combination Circuit

array	ρ_n ($\mu\Omega$ m)	ρ_m ($\mu\Omega$ m)	ρ_s ($\mu\Omega$ m)	ρ_0 ($\mu\Omega$ m)	Δ_0 (meV)	ω	η	T_0 (K)	T_c^{offset} (K)
NDA1	0.09	0.46	0.06	66.1	0.8	0.17	10.9	4×10^{-7}	1.5
NDA2	0.34	0.14	0.03	65.2	0.8	0.19	5.2	1×10^{-7}	1
CDF	8.26	0	8213	0	0.1	0.5	3.25	–	2.8

We used a series–parallel combination circuit to model the disordered nanodiamond arrays. In the three-resistor circuit (see inset to Figure 6D), ρ_N and ρ_S are connected in parallel to represent the black nanodiamonds, and ρ_R is connected in series to represent the intergrain DLC. Accordingly, the circuit has a total resistivity of

$$\rho_{\text{total}} = \frac{\rho_N \rho_S}{\rho_N + \rho_S} + \rho_R \quad (3)$$

Taking advantage of the switch-like function of the parallel-connected resistors, the dominance of intragrain electrical transport is transferred from the single quasiparticle resistor ρ_N (the fermionic channel) to the “superconducting” resistor ρ_S (the bosonic channel) upon the bosonic phase transition.³⁴ To describe the Cooper pairing process, in which single quasiparticles around the Fermi level are removed from the fermionic channel to charge the bosonic channel, we write ρ_N as³⁵

$$\rho_N = \rho_n \left[-2 \int_{\Delta(T)}^{\infty} g(E) f'(E) dE \right]^{-1} \quad (4)$$

where

$$\Delta(T) = \Delta_0 \left(1 - \frac{T}{T_c^{\text{onset}}} \right)^\omega \quad (5)$$

is taken to approximate the half width of the superconducting gap (in Bardeen–Cooper–Schrieffer theory, $\omega = 0.5$ when T is close to T_c), $g(E) = E/[E^2 - \Delta(T)^2]^{1/2}$ is the single quasiparticle DOS in Bardeen–Cooper–Schrieffer theory, and $f'(E)$ is the derivative of the Fermi–Dirac distribution. The bosonic phase transition at T_c^{offset} can be empirically written as^{34,35}

$$\rho_S = \rho_m + \rho_s \left(\frac{T}{T_c^{\text{offset}}} - 1 \right)^\eta \quad (6)$$

For ρ_R , Mott’s law in 3D has already been proven to be a fairly good description of the disordered DLC in spite of the deviation below 1 K (see Figure 4). Consistently, we use eq 2 for the expression of ρ_R . To perform the theoretical modeling, $T_c^{\text{onset}} = 9$ K is used for all the three arrays, $T_c^{\text{offset}} = 2.8$ K is fixed for CDF, and ρ_n , ρ_m , ρ_s , ρ_0 , Δ_0 , ω , η , and T_0 are left as fitting parameters, together with the T_c^{offset} of NDA1 and NDA2. As shown in Figure 6D, despite our limited knowledge of the physical meaning of the values of some fitting parameters (see Table 1), all three nanodiamond arrays are fairly well described by using the three-resistor circuit model, and reasonable values are obtained for the key variables such as Δ_0 , ω , and the T_c^{offset} of NDA1 and NDA2. Note that owing to $\rho_0 = 0$, ρ_R is eliminated from eq 3 for the modeling of CDF, meaning that the influence of DLC is neglected in this case. We emphasize that, practically, the local critical temperatures of individual nanodiamonds are different as revealed by the STM/S data (see Figure 6A), while, in our simplified model, the

nanodiamonds are described with the same set of parameters, which can be the cause of the deviations of the fitting results from the experimental data.

CONCLUSION

To conclude, we have prepared nanodiamond-DLC hybrid arrays for investigations of bosonic confinement and coherence in the presence of disorder. Our data demonstrate that, when increasing the degree of disorder (the dispersion of intergrain spacing), the low-temperature superconducting state transforms into bosonic dirty metallic states, due to the breaking of global phase coherence and the persistence of localized Cooper pairs. Our direct local measurement data suggest the evolution of the superconducting gap from U-shaped to V-shaped and the disappearance of coherence peaks in the LDOS as the evidence for the intragrain confinement of Cooper pairs. Our observation of the wide ranging local critical temperature, in spite of the homogeneous boron doping, brings attention to the intragrain crystallographic defects such as twinning, which can be viewed as another set of disorder at scales much smaller than the grain size. The influence of the intragrain defects on the superconducting order parameter deserves further study.

EXPERIMENTAL SECTION

Samples. The nanodiamond-DLC-nanodiamond arrays were prepared using hot filament chemical vapor deposition (CVD). Si/SiO₂ substrates were seeded with diamond nanoparticles (diameter ~20 nm), to generate nucleation sites for subsequent diamond growth. Colloidal suspensions of diamond nanoparticles dispersed in ethanol with two different degrees of dilution were used, that is, 0.2 g L⁻¹ for CDF and 20 μ g L⁻¹ for NDA1 and NDA2. After immersing the Si/SiO₂ substrates in the colloidal suspensions (10 min for CDF, 10 min for NDA1, and 270 min for NDA2), the substrates with different seeding densities (3×10^{10} cm⁻² for CDF, 2×10^7 cm⁻² for NDA1, and 2×10^8 cm⁻² for NDA2, as estimated using scanning electron microscopy) were spray-dried with a spinner and then placed into the CVD reactor for the diamond growth. A gas mixture, 0.6% CH₄ in H₂ at 20 Torr pressure, was thermally dissociated using a tantalum filament at 2200 °C situated 3 mm above the samples, which were maintained at 800 °C by an independent substrate heater. Boron doping was obtained by adding diborane (B₂H₆) to the gas mixture with a B₂H₆/CH₄ ratio of 5%. After 40 min deposition, the sample with the highest seeding density had coalesced into a continuous boron-doped polycrystalline diamond film (sample CDF) with a thickness of ~600 nm. In contrast, the diamond seeds in the two samples with sparser seeding density (NDA1 and NDA2) had increased in size, but remained as separate diamond particles, while the regions of exposed Si/SiO₂ between the grains had become coated in a ~180 nm-thick layer of amorphous carbon or DLC. The samples were grown in a H₂-rich atmosphere and were cooled down in H₂ gas after deposition. This ensures that the diamond surface is hydrogen terminated.^{36–40} All samples were prepared in one batch to avoid batch-to-batch variability.

Taking into account the minute volume ratio of nanodiamond to DLC in NDA1, we performed Hall effect measurements on NDA1 to estimate the electron mobility of the DLC, $\mu_n = 1441$ cm² V⁻¹ s⁻¹ at 3 K, from which the diffusion coefficient D was deduced.

Statistics of the intergrain spacing and the grain size distribution were obtained by analyzing the large-area SEM images of the arrays

with software Nano Measurer (Jie Xu, Fudan University, China). The intergrain spacings of NDA1 and NDA2 were measured *via* triangular tessellation of the SEM images.

STEM-EELS Measurements and ADF-STEM Imaging. Transmission electron microscopy (TEM) lamellae were prepared by focused ion beam milling for structural analysis in Jülich and Antwerp with different setups. To protect the nanodiamond surface from ion beam damage, a layer of Pt was deposited prior to the ion milling. In Jülich, aberration-corrected dark-field scanning transmission electron microscopy (ADF-STEM) and spatially resolved electron energy-loss spectroscopy (EELS) were carried out at 80 kV and 200 kV, respectively, on an FEI Titan G2 80-200 ChemiSTEM microscope equipped with a high-brightness Schottky field emission electron gun, a probe Cs corrector, and a Gatan Enfium 977 ER spectrometer. ADF-STEM images were acquired using a convergence semiangle of 24.7 mrad and an inner collection semiangle of 29 mrad. EELS spectrum imaging was conducted using dual-EELS spectroscopy mode with a convergence semiangle of 17.7 mrad, a collection semiangle of 52 mrad, and a dispersion of 0.1 eV. Energy shift was corrected using the simultaneously acquired zero-loss spectra. Plural scattering was removed by Fourier-ratio method. In Antwerp, STEM was performed at FEI cubed Titan equipped with probe corrector using acceleration voltage of 300 kV. EELS was performed at 300 kV making use of Gatan Enfium electron spectrometer integrated into the cubed Titan. ADF imaging was carried out with a convergence semiangle α of ~ 21 mrad. STEM-EELS maps were obtained with the same convergence angle and with collection angle of ~ 100 mrad. Quantitative estimation of the boron concentration was made using the EELS model software with parameters of convergence angle 20 mrad, collection angle 80 mrad, and spectra energy resolution 1 eV.

Electrical Transport Measurements. A Heliox ^3He cryostat (Oxford Instruments) and a physical property measurement system (Quantum Design) were used for the measurements of the electrical transport properties of the samples. The 3D nature of all the three samples was confirmed by the same results obtained from measurements in perpendicular and parallel magnetic fields.

STM/S Measurements. The LDOS was measured using a sub-Kelvin scanning tunneling microscopy (STM) system. Atomically sharp STM tips were formed *in situ* by controlled contact of the Au tip with a clean Au surface at cryogenic temperatures.⁴¹ The bias voltage was applied to the tip, while the sample was grounded. The I - V spectra were recorded with a feedback loop off, and the initial tunneling resistance was 10 M Ω . The differential conductance curves were numerically derived from the I - V measurements.

ASSOCIATED CONTENT

Supporting Information

The Supporting Information is available free of charge on the ACS Publications website at DOI: 10.1021/acsnano.7b07148.

Additional information on the statistical analysis of the grain size distribution of the nanodiamond arrays, determination of ξ_{CL} from the $\mu_0 H_{c2}$ - T phase boundary of CDF, and STM/S data (PDF)

AUTHOR INFORMATION

Corresponding Authors

*E-mail: sp3.zhang@gmail.com.

*E-mail: victor.moshchalkov@kuleuven.be.

ORCID

Gufei Zhang: 0000-0002-0150-5452

Hongchu Du: 0000-0002-4661-4644

Paul W. May: 0000-0002-5190-7847

Haifeng Yuan: 0000-0001-6652-3670

Johan Hofkens: 0000-0002-9101-0567

Author Contributions

[†]These authors contributed equally.

Notes

The authors declare no competing financial interest.

ACKNOWLEDGMENTS

G.Z., J.V.A., and V.V.M. acknowledge support from the Methusalem Funding by the Flemish Government. G.Z. and H.Y. are postdoctoral research fellows of the FWO (Research Foundation-Flanders). T.S., O.O., P.S.Z., J.K., and P.S. are supported by APVV-0036-11, APVV-14-0605, VEGA 1/0409/15, VEGA 2/0149/16, and EU ERDF-ITMS 26220120005. H.D. and R.E.D. thank Doris Meertens for preparation of the TEM lamellae by FIB. H.D. acknowledges support from the DFG (SFB917). G.Z. thanks Svetlana Korneychuk and Johan Verbeeck for additional STEM measurements. P.W.M. thanks the UK EPSRC for funding. The authors thank Richard Hlubina for helpful discussions about the STM/S data.

REFERENCES

- (1) May, P. W. Diamond Thin Films: A 21-st Century Material. *Philos. Trans. R. Soc., A* **2000**, 358, 473–495.
- (2) Syamsul, M.; Kitabayashi, Y.; Matsumura, D.; Saito, T.; Shintani, Y.; Kawarada, H. High Voltage Breakdown (1.8 kV) of Hydrogenated Black Diamond Field Effect Transistor. *Appl. Phys. Lett.* **2016**, 109, 203504.
- (3) Kusterer, J.; Kohn, E.; Lüker, A.; Kirby, P.; O'Keefe, M. F. Diamond High Speed and High Power MEMS Switches. Proceedings from the 4th EMRS DTC Technical Conference, July 10-11, 2007, Edinburgh, UK; EMRS DTC: Edinburgh, UK, 2007; p A26.
- (4) Kuball, M.; Pomeroy, J. W.; Calvo, J. A.; Sun, H.; Simon, R. B.; Francis, D.; Fails, F.; Twitchen, D.; Rossi, S.; Alomari, M.; Kohn, E.; Tóth, L.; Pécz, B. Novel Thermal Management of GaN Electronics: Diamond Substrates. Proceedings from the ASME International Technical Conference and Exhibition on Packaging and Integration of Electronic and Photonic Microsystems collocated with the ASME 13th International Conference on Nanochannels, Microchannels, and Minichannels, July 6–9, 2015, San Francisco, CA; ASME: New York, 2015. DOI:10.1115/IPACK2015-48145.
- (5) Zhang, G.; Turner, S.; Ekimov, E. A.; Vanacken, J.; Timmermans, M.; Samuely, T.; Sidorov, V. A.; Stishov, S. M.; Lu, Y.; Deloof, B.; Goderis, B.; Van Tendeloo, G.; Van de Vondel, J.; Moshchalkov, V. V. Global and Local Superconductivity in Boron-Doped Granular Diamond. *Adv. Mater.* **2014**, 26, 2034–2040.
- (6) Ekimov, E. A.; Sidorov, V. A.; Bauer, E. D.; Mel'nik, N. N.; Curro, N. J.; Thompson, J. D.; Stishov, S. M. Superconductivity in Diamond. *Nature* **2004**, 428, 542–545.
- (7) Takano, Y.; Nagao, M.; Sakaguchi, I.; Tachiki, M.; Hatano, T.; et al. Superconductivity in Diamond Thin Films Well Above Liquid Helium Temperature. *Appl. Phys. Lett.* **2004**, 85, 2851–2853.
- (8) Mandal, S.; Bautze, T.; Williams, O. A.; Naud, C.; Bustarret, É.; Omnès, F.; Rodière, P.; Meunier, T.; Bäuerle, C.; Saminadayar, L. The Diamond Superconducting Quantum Interference Device. *ACS Nano* **2011**, 5, 7144–7148.
- (9) Blase, X.; Bustarret, E.; Chapelier, C.; Klein, T.; Marcenat, C. Superconducting Group-IV Semiconductors. *Nat. Mater.* **2009**, 8, 375–382.
- (10) Bustarret, E. Superconducting Diamond: An Introduction. *Phys. Status Solidi A* **2008**, 205, 997–1008.
- (11) Zhang, G.; Janssens, S. D.; Vanacken, J.; Timmermans, M.; Vacík, J.; Ataklti, G. W.; Decelle, W.; Gillijns, W.; Goderis, B.; Haenen, K.; Wagner, P.; Moshchalkov, V. V. Role of Grain Size in Superconducting Boron-Doped Nanocrystalline Diamond Thin Films Grown by CVD. *Phys. Rev. B: Condens. Matter Mater. Phys.* **2011**, 84, 214517.
- (12) Fisher, M. P. A. Quantum Phase Transitions in Disordered Two-Dimensional Superconductors. *Phys. Rev. Lett.* **1990**, 65, 923–926.

- (13) Baturina, T. I.; Mironov, A. Yu.; Vinokur, V. M.; Baklanov, M. R.; Strunk, C. Localized Superconductivity in the Quantum-Critical Region of the Disorder-Driven Superconductor-Insulator Transition in TiN Thin Films. *Phys. Rev. Lett.* **2007**, *99*, 257003.
- (14) Sacépé, B.; Chapelier, C.; Baturina, T. I.; Vinokur, V. M.; Baklanov, M. R.; Sanquer, M. Disorder-Induced Inhomogeneities of the Superconducting State Close to the Superconductor-Insulator Transition. *Phys. Rev. Lett.* **2008**, *101*, 157006.
- (15) Vinokur, V. M.; Baturina, T. I.; Fistul, M. V.; Mironov, A.; Yu; Baklanov, M. R.; Strunk, C. Superinsulator and Quantum Synchronization. *Nature* **2008**, *452*, 613–615.
- (16) Sacépé, B.; Dubouchet, T.; Chapelier, C.; Sanquer, M.; Ovadia, M.; Shahar, D.; Feigel'man, M.; Ioffe, L. Localization of Preformed Cooper Pairs in Disordered Superconductors. *Nat. Phys.* **2011**, *7*, 239–244.
- (17) White, A. E.; Dynes, R. C.; Garno, J. P. Destruction of Superconductivity in Quench-Condensed Two-Dimensional Films. *Phys. Rev. B: Condens. Matter Mater. Phys.* **1986**, *33*, 3549–3552.
- (18) Valles, J. M., Jr.; Hsu, S.-Y.; Dynes, R. C.; Garno, J. P. Electron Tunneling Studies of Ultrathin Films near the Superconductor-to-Insulator Transition. *Phys. B* **1994**, *197*, 522–529.
- (19) Rimberg, A. J.; Ho, T. R.; Kurdak, Ç.; Clarke, J.; et al. Dissipation-Driven Superconductor-Insulator Transition in a Two-Dimensional Josephson-Junction Array. *Phys. Rev. Lett.* **1997**, *78*, 2632–2635.
- (20) Delsing, P.; Chen, C. D.; Haviland, D. B.; Harada, Y.; Claeson, T. Charge Solitons and Quantum Suctuations in Two-Dimensional Arrays of Small Josephson Junctions. *Phys. Rev. B: Condens. Matter Mater. Phys.* **1994**, *50*, 3959–3971.
- (21) Benz, S. P.; Forrester, M. G.; Tinkham, M.; Lobb, C. J. Positional Disorder in Superconducting Wire Networks and Josephson Junction Arrays. *Phys. Rev. B: Condens. Matter Mater. Phys.* **1988**, *38*, 2869–2872.
- (22) Hollen, S. M.; Nguyen, H. Q.; Rudisaile, E.; Stewart, M. D., Jr.; Shainline, J.; Xu, J. M.; Valles, J. M., Jr. Cooper-Pair Insulator Phase in Superconducting Amorphous Bi Films Induced by Nanometer-Scale Thickness Variations. *Phys. Rev. B: Condens. Matter Mater. Phys.* **2011**, *84*, 064528.
- (23) Eley, S.; Gopalakrishnan, S.; Goldbart, P. M.; Mason, N. Approaching Zero-Temperature Metallic States in Mesoscopic Superconductor–Normal–Superconductor Arrays. *Nat. Phys.* **2011**, *8*, 59–62.
- (24) Han, Z.; Allain, A.; Arjmandi-Tash, H.; Tikhonov, K.; Feigel'man, M.; Sacépé, B.; Bouchiat, V. Collapse of Superconductivity in a Hybrid Tin–Graphene Josephson Junction Array. *Nat. Phys.* **2014**, *10*, 380–386.
- (25) Bustarret, E.; Achatz, P.; Sacépé, B.; Chapelier, C.; Marcenat, C.; Ortéga, L.; Klein, T. Metal-Insulator Transition and Superconductivity in Boron-Doped Diamond. *Philos. Trans. R. Soc., A* **2008**, *366*, 267–279.
- (26) Saint-James, D.; Sarma, G.; Thomas, E. J. Surface Superconductivity. In *Type II Superconductivity*; Pergamon Press: Oxford, 1969; pp 117–120.
- (27) Resnick, D. J.; Garland, J. C.; Boyd, J. T.; Shoemaker, S.; Newrock, R. S. Kosterlitz-Thouless Transition in Proximity-Coupled Superconducting Arrays. *Phys. Rev. Lett.* **1981**, *47*, 1542.
- (28) Kirzhner, T.; Koren, G. Pairing and the Phase Diagram of the Normal Coherence Length $\xi_N(T, x)$ Above T_c of $\text{La}_{2-x}\text{Sr}_x\text{CuO}_4$ Thin Films Probed by the Josephson Effect. *Sci. Rep.* **2015**, *4*, 6244.
- (29) Shklovski, B. I.; Efros, A. L. Variable-Range Hopping Conduction. In *Electronic Properties of Doped Semiconductors*; Springer-Verlag: Berlin, 1984; pp 202–222.
- (30) Dubrovinskaia, N.; Wirth, R.; Wosnitza, J.; Papageorgiou, T.; Braun, H. F.; Miyajima, N.; Dubrovinsky, L. An Insight into What Superconducts in Polycrystalline Boron-Doped Diamonds Based on Investigations of Microstructure. *Proc. Natl. Acad. Sci. U. S. A.* **2008**, *105*, 11619–11622.
- (31) Feigel'man, M. V.; Ioffe, L. B.; Kravtsov, V. E.; Yuzbashyan, E. A. Eigenfunction Fractality and Pseudogap State near the Superconductor-Insulator Transition. *Phys. Rev. Lett.* **2007**, *98*, 027001.
- (32) Takano, Y. Superconductivity in CVD Diamond Films. *J. Phys.: Condens. Matter* **2009**, *21*, 253201.
- (33) Zhang, G.; Vanacken, J.; Van de Vondel, J.; Decelle, W.; Fritzsche, J.; Moshchalkov, V. V.; Willems, B. L.; Janssens, S. D.; Haenen, K.; Wagner, P. Magnetic Field-Driven Superconductor–insulator Transition in Boron-Doped Nanocrystalline Chemical Vapor Deposition Diamond. *J. Appl. Phys.* **2010**, *108*, 013904.
- (34) Zhang, G.; Samuely, T.; Kačmarčík, J.; Ekimov, E. A.; Li, J.; Vanacken, J.; Szabó, P.; Huang, J.; Pereira, P. J.; Cerbu, D.; Moshchalkov, V. V. Bosonic Anomalies in Boron-Doped Polycrystalline Diamond. *Phys. Rev. Appl.* **2016**, *6*, 064011.
- (35) Zhang, G.; Zeleznik, M.; Vanacken, J.; May, P. W.; Moshchalkov, V. V. Metal-Bosonic Insulator-Superconductor Transition in Boron-Doped Granular Diamond. *Phys. Rev. Lett.* **2013**, *110*, 077001.
- (36) Maier, F.; Riedel, M.; Mantel, B.; Ristein, J.; Ley, L. Origin of Surface Conductivity in Diamond. *Phys. Rev. Lett.* **2000**, *85*, 3472–3475.
- (37) Ristein, J. Surface Science of Diamond: Familiar and Amazing. *Surf. Sci.* **2006**, *600*, 3677–3689.
- (38) Bolker, A.; Saguy, C.; Kalish, R. Transfer Doping of Single Isolated Nanodiamonds, Studied by Scanning Probe Microscopy Techniques. *Nanotechnology* **2014**, *25*, 385702.
- (39) Edmonds, M. T.; Pakes, C. I.; Ley, L. Self-Consistent Solution of the Schrödinger-Poisson Equations for Hydrogen-Terminated Diamond. *Phys. Rev. B: Condens. Matter Mater. Phys.* **2010**, *81*, 085314.
- (40) Natsui, K.; Yamamoto, T.; Watanabe, T.; Kamihara, Y.; Einaga, Y. Modulation of Critical Current Density in Polycrystalline Boron-Doped Diamond by Surface Modification. *Phys. Status Solidi B* **2013**, *250*, 1943–1949.
- (41) Samuely, T.; Szabó, P.; Komanický, V.; Rodrigo, J.; Vieira, S.; Samuely, P. Enhanced Superconductivity in Nanosized Tips of Scanning Tunneling Microscope. *Acta Phys. Pol., A* **2010**, *118*, 1038.